ARTICLE

Fault identification and enhancement using residual U-Net: Application to field seismic data

Jianhua Wang[1]*, **Cong Niu**[1], **Yandong Wang**[1], **Yun Ling**[1], **Di Wang**[1], **Xiuping Jiang**[2,3,4], and **Chenshuo Yuan**[2]

[1]CNOOC Research Institute Co., Ltd., Beijing, China

[2]College of Marine Geo-sciences, Ocean University of China, Qingdao, Shandong, China

[3]Qingdao National Laboratory for Marine Science and Technology, Qingdao, Shandong, China

[4]Key Laboratory of Submarine Geosciences and Prospecting Techniques, Ministry of Education, Ocean University of China, Qingdao, Shandong, China

Abstract

Fault identification is a critical step in seismic data interpretation. Traditional fault identification methods rely heavily on manual interpretation, which is inefficient and significantly influenced by subjective factors. This paper proposes a fault identification algorithm based on a Residual U-Net–curvelet hybrid framework. By introducing residual learning strategies and applying batch normalization and skip connection techniques, the generalization ability and convergence speed of the network are enhanced, thereby improving the accuracy and efficiency of fault identification. Results from field data processing demonstrate that this method achieves high identification accuracy under complex geological structures and low signal-to-noise ratio conditions, providing reliable fault identification results for efficient seismic data interpretation.

*Corresponding author:
Jianhua Wang
(wangjh7@cnooc.com.cn)

Publisher's Note: AccScience Publishing remains neutral with regard to jurisdictional claims in published maps and institutional affiliations.

1. Introduction

Fault identification is a critical aspect of seismic data interpretation, particularly in oil and gas exploration and development. Accurate fault identification holds significant importance for structural interpretation, reservoir prediction, and analysis of hydrocarbon migration pathways.

However, traditional fault identification methods rely heavily on the experience of interpreters and use seismic attributes or structural features for recognition, which are labor-intensive, highly subjective, and sensitive to noise. These limitations make it difficult to meet the demands of detailed interpretation, particularly in complex geological settings or in seismic data with low signal-to-noise ratios (SNR), where the ability to identify small faults is often inadequate. Therefore, achieving automated, rapid, and high-precision fault identification has become an urgent research problem.

With the advancement of seismic-attribute technology, fault-identification methods include attribute-based classifiers, such as coherence cubes,[1,2] variance cubes,[3] curvature

attributes,[4,5] the C3-coherence technique,[2] and fault-likelihood measures;[6,7] fault-enhancement approaches, such as ant tracking,[8] structure-oriented filtering,[9] and optimal surface voting;[10] as well as hybrid workflows that combine variance cubes with high-definition ant tracking. However, these approaches are highly dependent on data quality: While they can be effective in shallow sections, their performance degrades for deep, low-quality seismic data and in structurally complex or heavily faulted areas, where inferred fault continuity is poor, and the solutions are strongly non-unique, often diminishing their interpretational value.

In recent years, with the rapid development of artificial intelligence (AI) technology, the application of AI to achieve automatic, fast, and accurate fault identification—overcoming the subjective influence of manual interpretation—has gradually become an important research direction in the field of oil and gas geophysical exploration and development.

Early studies primarily adopted relatively simple architectures, such as AlexNet and VGGNet,[11] but their accuracy in fault identification was limited. Later, researchers introduced residual network (ResNet)-based models[12]—by leveraging residual learning to mitigate deep-network degradation and vanishing gradients, these models improved fault-detection accuracy. Nevertheless, such approaches are constrained by fixed input-size requirements and a bias toward local feature extraction, resulting in poorer performance for small-scale faults. Wu *et al.*[13] employed a convolutional neural network for fault identification and subsequently constructed anisotropic Gaussian functions to estimate the fracture dip and azimuthal extent. However, because the model is trained on local image patches and extracts features only within small-scale neighborhoods, its computational efficiency is significantly limited.

Fully convolutional neural networks achieved the first end-to-end breakthrough in image recognition.[14] U-Net[15,16] introduced an architectural innovation that couples multi-scale feature extraction in the encoder with precise localization in a symmetric decoder and, via skip connections, enables cross-level fusion of shallow details and deep semantic features,[17] thereby markedly improving fault-identification accuracy. Moreover, integrating U-Net with ResNet to form residual U-Net (ResU-Net) increases network depth and further enhances fault-detection performance.[18] Unlike the classical U-Net—which adopts a symmetric encoder–decoder built from convolution–batch normalization–rectified linear unit (ReLU) stacks and conveys spatial details via skip connections—the residual U-Net introduces residual blocks within each

stage. While preserving U-Net's original skip connections and precise localization capability, it significantly improves gradient flow and feature reuse, making the network easier to deepen and more stable to train. Consequently, it is more robust under low-SNR and complex structural settings: It converges faster, is more sensitive to weak/narrow faults, reduces false positives, and improves generalization and fault identification/detection accuracy.

To further reduce the subjectivity of manual fault identification and enhance the accuracy of identifying micro-faults, this study develops a fault detection model utilizing a ResU-Net architecture–curvelet hybrid framework, designed to learn the complex non-linear mapping between seismic amplitude data and fault probability distributions. In addition, fault information is enhanced using multi-scale component extraction and curvelet domain filtering techniques, thereby providing a solid foundation for subsequent interpretation and analysis.

2. Fault identification based on residual U-Net

2.1. Residual learning strategy for fault identification

By employing a residual U-Net, the sample space formed by fault-related seismic data is explored to construct a fault identification model that characterizes the mapping between seismic data and faults. In the fault identification task, the ResU-Net is trained with a hybrid loss function that combines cross-entropy and the Dice coefficient, and the evaluation metric is identification accuracy.

Compared to traditional fault-identification methods based on the U-Net convolutional neural network, the ResU-Net-based method not only adopts a different network architecture but also incorporates an improved loss function. The mathematical expression of the combined loss function is as follows:

$$\text{Dice} = \frac{2 \times \sum y \times \hat{y}}{\sum y + \sum \hat{y}} \tag{1}$$

$$\hat{L} = -\frac{1}{2}\Big[y \log \hat{y} + (1-y)\log(1-\hat{y}) \Big] - \text{Dice} \tag{2}$$

Where $\hat{L}$ represents the combined loss function, y denotes the fault labels of the true data, and $\hat{y}$ represents the predicted faults.

From a theoretical standpoint, the hybrid loss (cross-entropy/binary cross-entropy [BCE] + Dice coefficient) combines probability calibration with set-overlap optimization. BCE treats segmentation as per-pixel

log-likelihood maximization, yielding well-calibrated probabilities and sharp boundaries; because the Dice coefficient is normalized by the sizes of the foreground and the prediction, it is inherently robust to the class imbalance between thin fault traces and the vast background. Adding BCE provides stable, non-vanishing gradients in the early stage of training (when predictions are near zero) and helps prevent foreground over-expansion, thereby improving the precision–recall trade-off. In addition, in the ResU-Net-based fault-identification method, the neural network uses a sigmoid activation at the output layer and ReLU activations in the hidden layers.

2.2. Architecture of residual U-Net

This study employed the U-Net main structure, combined with batch normalization and residual learning concepts, to construct the ResU-Net, as shown in Figure 1. The network consists of four layers of upsampling and four layers of downsampling, each containing convolutional operations and batch normalization layers. The specific structural parameters vary slightly at different depths of the network. Each convolutional layer is immediately followed by batch normalization to optimize network performance and accelerate convergence. To maintain dimensional consistency between input and output tensors throughout the architecture, zero-padding is implemented in each convolutional layer to ensure that the input and output data dimensions remain the same.

The ResU-Net implements the residual learning strategy by adding an identity mapping (shown as "identity mapping" in Figure 1) between the input and output layers. In addition, to ensure rapid network convergence and avoid potential numerical issues, amplitude normalization is applied, scaling the seismic record amplitudes to the range [0, 1]. Consequently, the output layer of the neural network employs the sigmoid activation function, whose value range is [0, 1], with its mathematical expression provided in **Equation 3**. Furthermore, we applied a morphological dilation algorithm when creating the fault labels to make the fault locations more prominent, thereby improving the neural network's training efficiency. For the remaining layers, the ReLU activation function is used, and its mathematical expression is given in **Equation 4**. The loss function $\hat{L}$ of the ResU-Net is described in **Equation 2**, and the optimizer chosen is the adaptive gradient algorithm (Adagrad), which prevents oscillation during the later stages of training by adaptively reducing the learning rate.

$$S(x) = \frac{1}{1 + e^{-x}} \tag{3}$$

$$R(x) = \begin{cases} x & x > 0 \\ 0 & x \leq 0 \end{cases} \tag{4}$$

In the ResU-Net structure, each upsampling or downsampling stage is treated as a separate module. Skip connections link encoder and decoder modules that share the same spatial resolution, enabling direct transfer of corresponding feature maps. By channeling input image characteristics directly into the upsampling pathway, this structure enables precise spatial information transfer across network levels, thereby aiding in information reconstruction and accelerating convergence speed. The residual connections bridging input and output layers fundamentally modify the network's optimization objective, transitioning the learning paradigm from direct label prediction to residual mapping. This architectural innovation significantly enhances model performance by
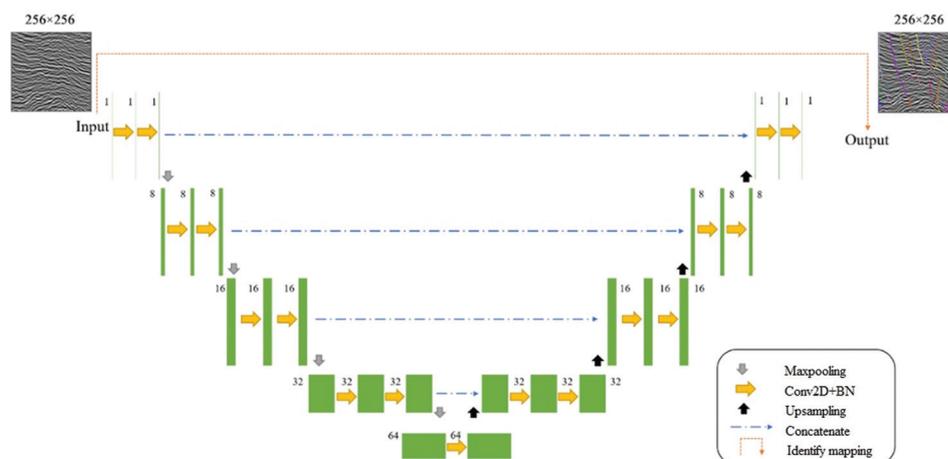

Figure 1. Residual U-Net structure
Abbreviations: BN: Batch normalization; Conv2D: 2D convolutional layer.

reducing the network's reliance on direct label fitting. As a result, the network captures more fault-related features, improving its generalization performance and mitigating overfitting.

We evaluated the computational complexity of the ResU-Net, as shown in Figure 1—input: $1 \times 256 \times 256$; channel progression: $1{\to}8{\to}16{\to}32{\to}64{\to}32{\to}16{\to}8$; each stage uses a residual block with two 3×3 convolutions followed by batch normalization; the decoder adopts bilinear upsampling and concatenates with encoder features. Based on standard formulas, the model contains approximately 0.20 M parameters (including batch normalization), with FP32 weights requiring about 0.8 MB, and it requires approximately 0.69 GFLOPs per forward pass per sample. Training uses the Adagrad optimizer; the parameter-related memory footprint is approximately four times the weight size (including weights, gradients, and optimizer statistics), totaling approximately 3.2 MB. Under FP32 with a batch size of $B = 4$, activation maps dominate memory usage at 35 ivatB; when framework caches and intermediate tensors are included, the peak training memory typically reaches 50ach0 MB. Overall, complexity scales approximately as O(HW) with input resolution and grows roughly linearly with channel width and depth, while residual shortcuts and bilinear upsampling introduce only negligible additional overhead.

The ResU-Net deep neural network, whose core structure relies on skip connections between the encoder and decoder, utilizes cropped seismic profiles as inputs and their corresponding interpreted fault images as labels. During the training phase, the model parameters undergo optimization, yielding a pre-trained network that subsequently performs comprehensive fault detection across all seismic profiles. Subsequently, the fault images undergo vectorization processing, which involves extracting a list of fault points (x_i, t_i), describing the fault location information based on the amplitude values of the sample points in the image. Here, i is the breakpoint index, x_i and t_i represent the spatial coordinates and travel time of the i-th breakpoint (where $1{\leq}i{\leq}I$), and I denotes the total number of fault points.

To clarify the configuration of the neural network, Table 1 presents the detailed parameter settings of the ResU-Net used in this study, including the kernel size, number of channels, stride, and activation function for each layer. The network consists of four downsampling and four upsampling modules, each comprising convolutional operations followed by batch normalization. Skip connections are incorporated between corresponding encoder and decoder layers to enhance the reconstruction capability of fault structures. To maintain consistent input and output dimensions, all convolutional layers adopt zero-padding (padding = "same"). In addition, residual connections are introduced to improve the stability and generalization ability of the model.

The process of fault identification based on the migrated data volume is described as follows: First, a ResU-Net deep neural network, as shown in Figure 1, is constructed, and a sample set is generated using the partial seismic profile and the corresponding interpreted fault image depicted in Figure 2, after which the neural network is trained. The number of training iterations was set to 5,000, and the Adagrad optimizer was used. A subset of 2,000 samples was randomly selected from the sample set and used for training. All experiments in this study were implemented using the PyTorch framework.

At this stage, the correlation between the predicted fault probabilities and the reference labels exceeds 80%, indicating effective fault identification with a compact network architecture and good computational efficiency. The correlation versus iteration curve is shown in Figure 3.

Table 1. Network structure parameters

Module number	Kernel size	Convolution depth	Activation function	Normalization method	Skip connection	Up/downsampling	Image size
1	3×3	1	ReLU	BN	9	Downsampling	256×256
2		8	ReLU		8	Downsampling	128×128
3		16	ReLU		7	Downsampling	64×64
4		32	ReLU		6	Downsampling	32×32
5		64	ReLU		None	None	16×16
6		32	ReLU		4	Upsampling	32×32
7		16	ReLU		3	Upsampling	64×64
8		8	ReLU		2	Upsampling	128×128
9		1	Sigmoid		1	Upsampling	256×256

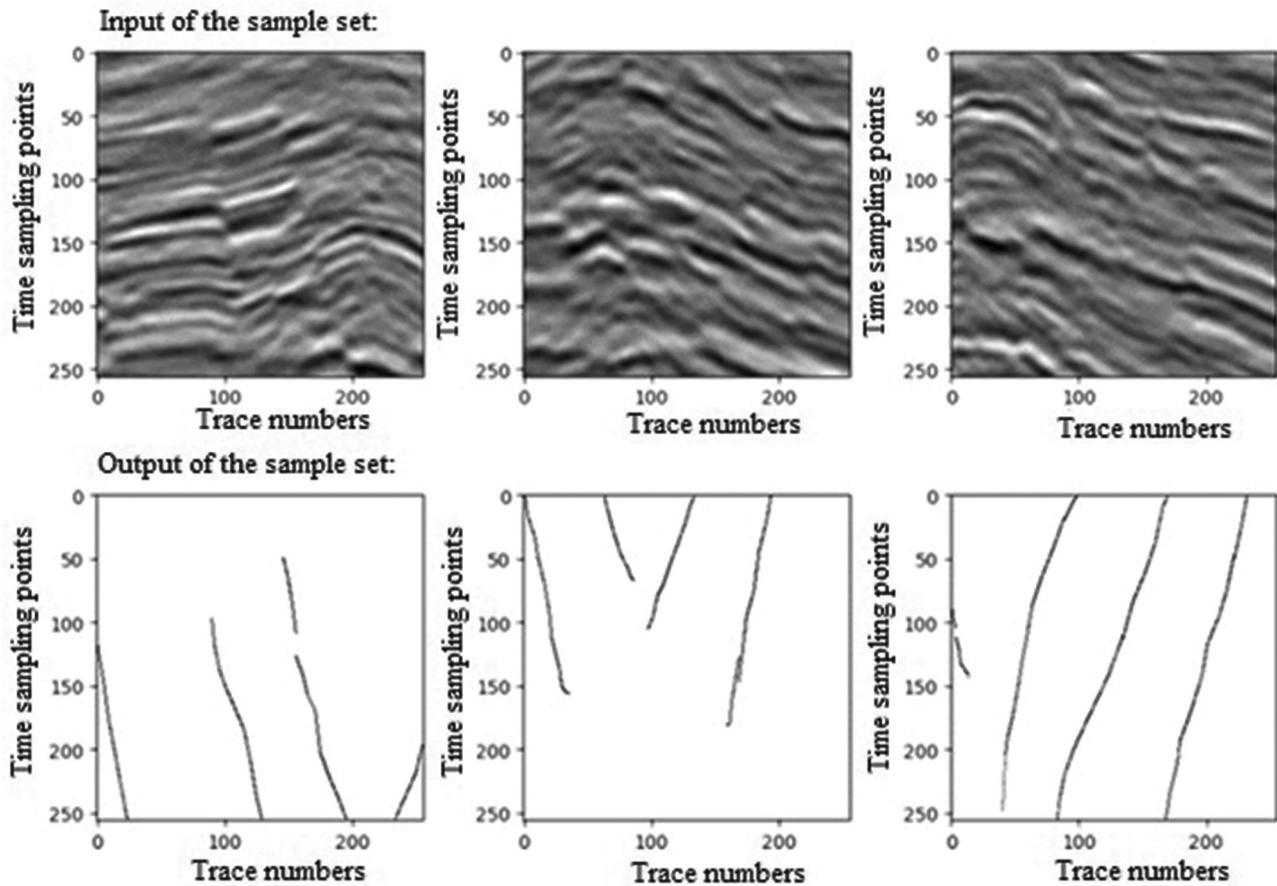Abbreviations: BN: Batch normalization; ReLU: Rectified linear unit.

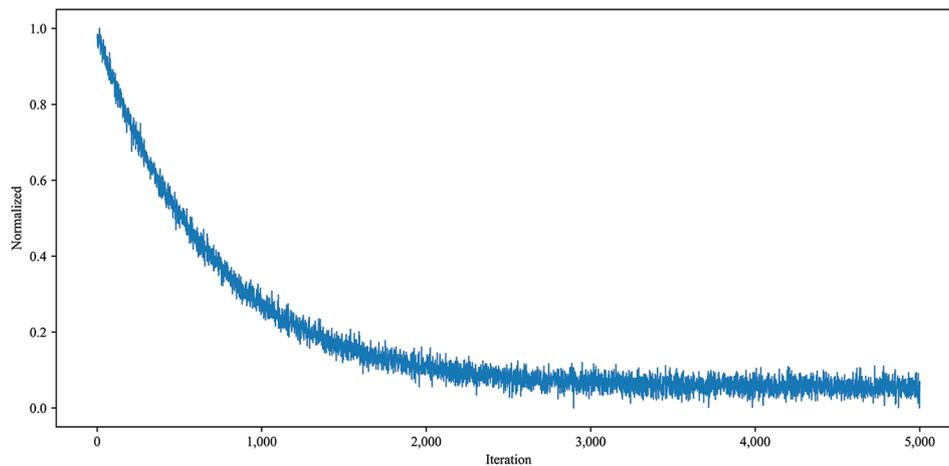**Figure 2.** Example of input and output of the sample set for neural network training

Figure 3. Correlation curve

3. Fault enhancement method based on multi-scale component extraction and filtering

During the acquisition process, seismic data are inevitably affected by factors, such as sensor sensitivity. The presence of noise and quantization errors during analog-to-digital conversion typically yields a diminished SNR. In seismic data processing, the limited spatial resolution of migration imaging methods and the difficulty of accurately positioning fault reflections often lead to "blurred fault points and

overlapping wavelets" in the migrated profiles. These issues significantly increase the difficulty of fault identification.

Directional filtering and edge-preserving filtering are commonly used techniques in image enhancement. The physical process involves smoothing the image using filters aligned with the local direction of the image, suppressing noise, and enhancing the continuity along the texture lines. The role of edge-preserving filtering is to protect the image edges during the filtering process, preventing edge information from becoming blurred due to filtering. These methods have been introduced into seismic data optimization, where directional filtering enhances the SNR and continuity of seismic wavelets. In addition, edge-preserving filtering preserves fault information, avoiding the blurring of faults caused by smoothing using data points on both sides of the fault. However, fundamentally, these methods belong to fault-preserving optimization techniques and cannot truly improve the imaging quality of fault structures. Therefore, they exhibit significant limitations in fault enhancement processing.

To address this issue, this study proposes a fault enhancement method based on multi-scale component extraction and filtering. The approach combines fault identification based on ResU-Net, calculation of fault enhancement filtering factors, and fault enhancement of multi-scale component data. It not only improves the accuracy of fault identification but also achieves high-precision fault enhancement processing for the imaging data volume, laying a solid foundation for subsequent interpretation and analysis.

3.1. Random noise suppression based on curvelet transform

The curvelet transform is composed of anisotropic curve-like basis elements, which can sparsely represent seismic data features. By applying thresholding to the coefficients in the curvelet domain, random noise can be effectively suppressed. This processing step significantly improves the SNR, making fault structures in the data more distinct. The curvelet transform is defined as the inner product between the seismic profile $s(x,t)$ and the curvelet function $\phi_{i,j,k}(x,t)$, and can be expressed as:

$$c(j,l,k) = \langle s, \varphi_{j,l,k} \rangle = \int_{x,t} s(x,t) \overline{\varphi_{j,l,k}(x,t)} dx dt \qquad (5)$$

Where $\langle \cdot, \cdot \rangle$ represents the inner product, $\phi_{j,l,k}(x)$ denotes the curvelet basis function at scale j, direction l, and position k, and $c(j,l,k)$ represents the curvelet coefficients obtained from the curvelet transform.

Among the obtained curvelet coefficients $c(j,l,k)$, a small number of large-amplitude coefficients represent the effective signal, while the majority of smaller-value coefficients indicate noise interference. Therefore, by zeroing out the smaller-amplitude coefficients and transforming back to the time–space domain, noise suppression can be achieved. By comparing the coefficients point by point, the maximum value c_{max} in $c(j,l,k)$ is obtained. Given a threshold parameter λ (where $0 < \lambda < c_{max}$), let:

$$c'(j,l,k) = \begin{cases} c(j,l,k), & |c(j,l,k)| \geq \lambda \\ 0, & |c(j,l,k)| < \lambda \end{cases} \qquad (6)$$

Where λ represents the threshold parameter.

To avoid damaging the effective signal, λ is generally chosen within the range $\lambda \in [0.01 c_{max}, 0.1 c_{max}]$.

The curvelet transform is a reversible mathematical transformation. Using the curvelet coefficients $c'(j,l,k)$, the noise-eliminated profile data $s'(x,t)$ can be reconstructed, expressed as:

$$s'(x,t) = \sum_{j,l,k} c'(j,l,k) \varphi_{j,l,k}(x,t) \qquad (7)$$

3.2. Fault information recovery in the migrated section

After attenuating random noise using the curvelet transform, fault information in the data is often compromised. To address this, it is necessary to restore the fault information based on the extracted breakpoint list (x_i, t_i). Since faults are large-angle structures, an interpolation method along the x-direction is employed to ensure a natural transition in the processed results. Let the interpolation width be Δx; then, the weighting factor for restoring fault information can be calculated as:

$$f(x,t_i) = \begin{cases} \dfrac{1}{\Delta x} |x - x_i|, & |x - x_i| < \Delta x \\ 1, & |x - x_i| \geq \Delta x \end{cases} \qquad (8)$$

Where $f(x,t_i)$ represents the weighting factor for fault information recovery.

The fault recovery result is obtained by performing a weighted summation of the filtered data and the original data using the weighting factor $f(x,t_i)$.

$$\tilde{s}(x,t_i) = s(x,t_i)\left[1 - f(x,t_i)\right] + s'(x,t_i) f(x,t_i) \qquad (9)$$

Where $\tilde{s}(x,t_i)$ represents the fault recovery result specifically for the breakpoint (x_i, t_i). By applying the weighted processing of **Equation 9** to all fault points in the

breakpoint list (x_i, t_i), the final fault recovery profile $\tilde{s}(x,t)$

is obtained.

3.3. Fault enhancement based on multi-scale components

Building on the multi-scale property of the curvelet transform, the profile data are further decomposed by scale. Let $\tilde{s}_n(x,t)$ denote the component obtained at scale n by retaining the corresponding curvelet coefficients and performing the inverse transform based on **Equation 7**.

By setting the scale factor g_n (where $0 \leq g_n \leq 1$) related to scale n, the filtering factor for the breakpoint list (x_i, t_i) can be defined as follows:

$$f_n(x,t_i) = \begin{cases} 1 - \dfrac{1-g_n}{\Delta x_n}|x - x_i|, & |x - x_i| < \Delta x_n \\ 1, & |x - x_i| \geq \Delta x_n \end{cases} \quad (10)$$

Where $f_n(x,t_i)$ represents the filtering factor for fault enhancement.

By applying the filtering factor $f_n(x,t_i)$ to the profile component $\tilde{s}_n(x,t)$ at scale n, fault-enhancement filtering can be performed, resulting in:

$$\tilde{s}'_n(x,t_i) = \tilde{s}_n(x,t_i) f_n(x,t_i) \quad (11)$$

Where $\tilde{s}'_n(x,t_i)$ represents the fault enhancement result specifically for the breakpoint (x_i, t_i). By applying the weighted processing of **Equation 12** to all fault points in the breakpoint list (x_i, t_i), the final processed result $\tilde{s}'_n(x,t)$ is obtained.

By synthesizing the multi-scale component data of fault enhancement into a single profile, the final fault enhancement result is obtained, expressed as:

$$\tilde{s}'(x,t) = \sum_{n=1}^{N} \tilde{s}'_n(x,t) \quad (12)$$

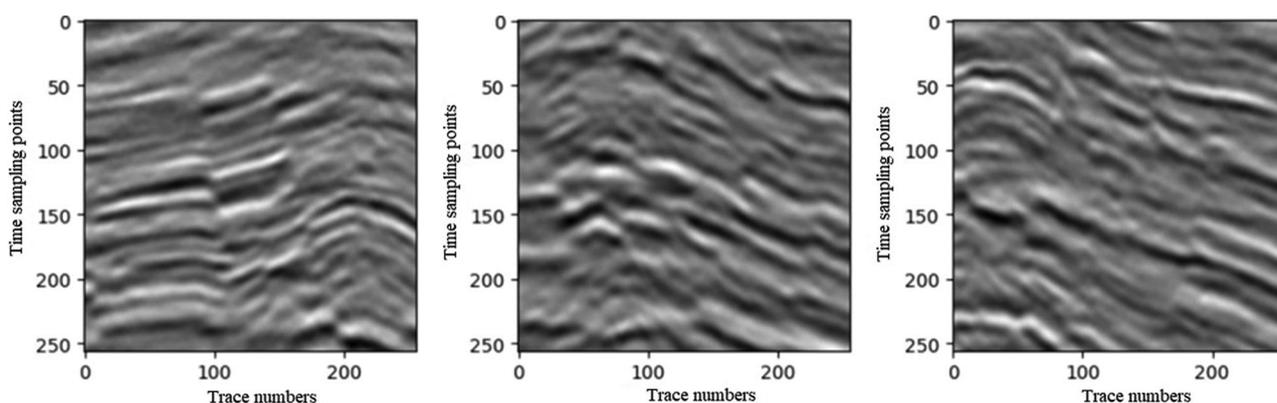Where $\tilde{s}'(x,t)$ represents the fault-enhanced profile

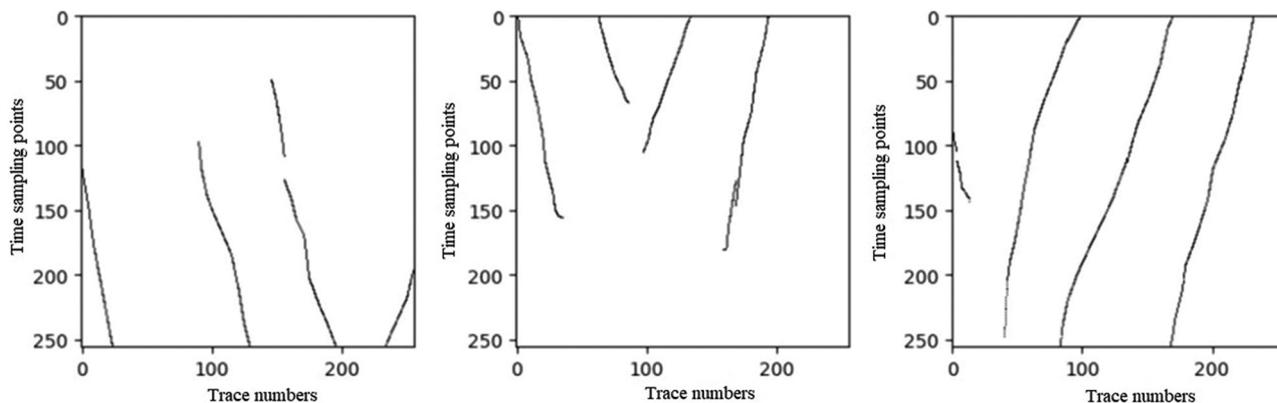**Figure 4.** Input of the sample set (neural network inputs)

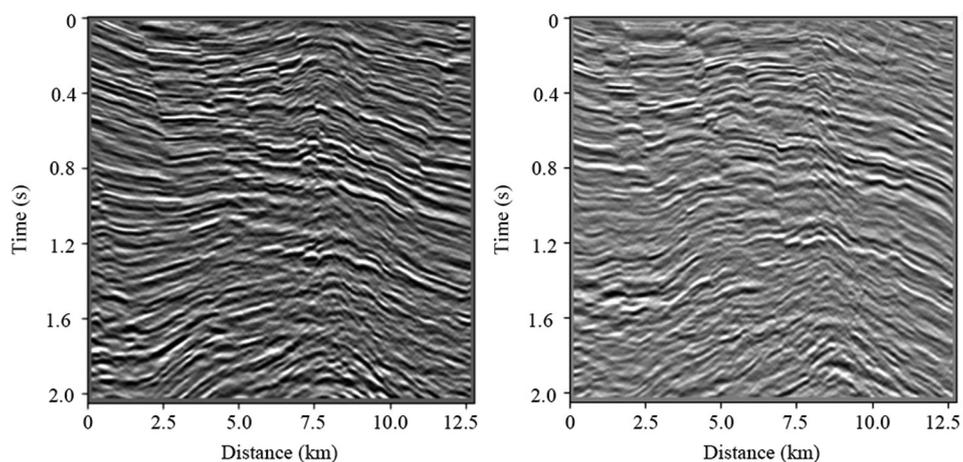**Figure 5.** Output of the sample set, with the black lines indicating the fault area

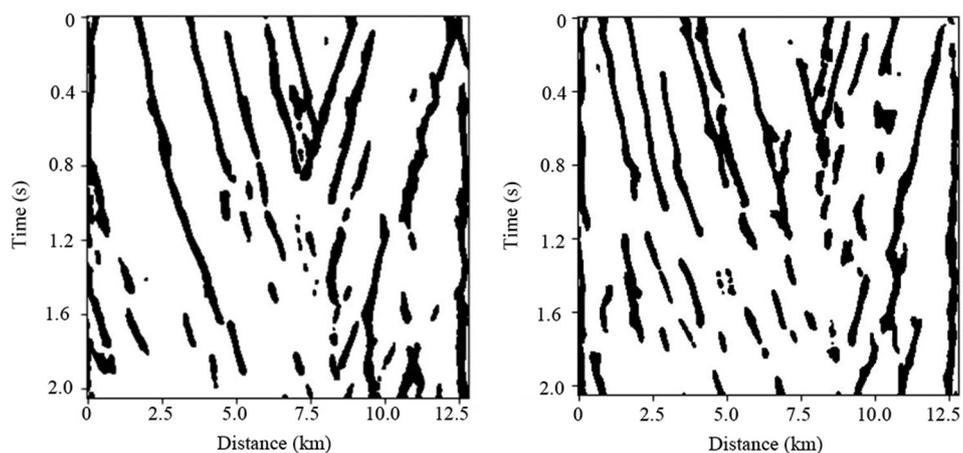**Figure 6.** Example seismic profile used for fault prediction (neural network inputs)

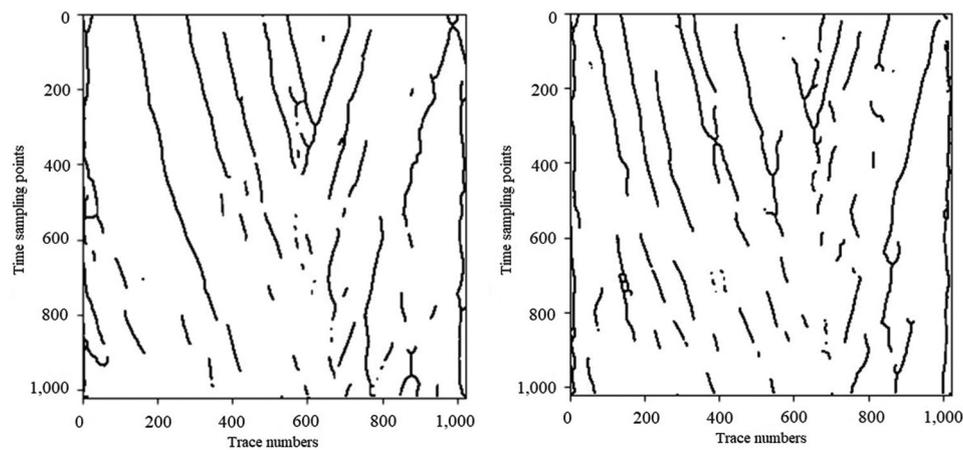**Figure 7.** Predicted fault probability image based on the input profile shown in Figure 6

Figure 8. Fault skeleton image extracted via multi-scale analysis in the curvelet domain, with the black lines indicating the fault skeleton
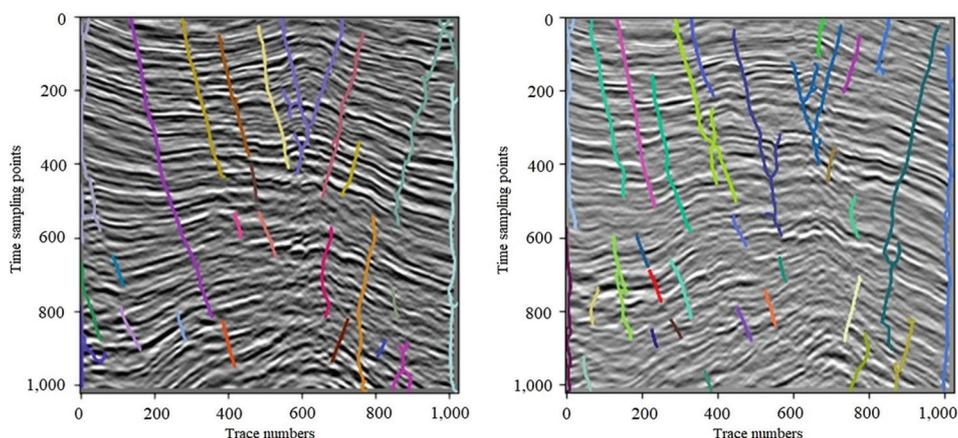
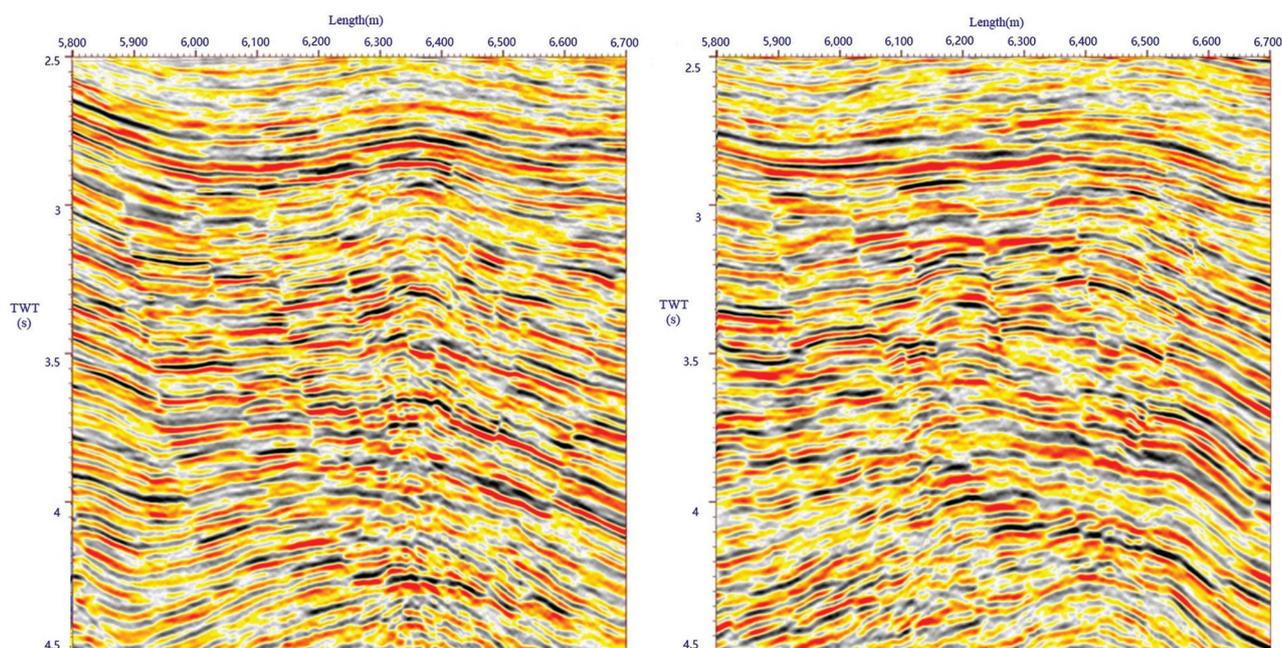**Figure 9.** Fault spatial location information extracted via contour tracing technology, with the colored lines indicating the fault traces

Figure 10. Imaging profile
Abbreviation: TWT: Two-way travel time.

obtained after multi-scale component extraction and filtering.

4. Effect analysis

4.1. Fault identification effect analysis of work area data

To assess performance on field data, a structural area in the East China Sea was employed as a case study. The imaging profiles and manually picked faults in this area were cropped into 256 × 256 patches to construct the sample set for training and evaluation (representative samples are shown in Figures 4 and 5).

A training dataset comprising 2,000 samples was randomly selected from the original sample set. After training and fine-tuning the neural network parameters, the optimized pre-trained model was applied to detect faults in the migrated section data of the target work area. The input seismic profiles and the corresponding fault predictions are illustrated in Figures 6 and 7, respectively.

Subsequently, fault skeleton extraction based on multi-scale analysis in the curvelet domain was performed on the fault probability image, resulting in the fault skeleton image as shown in Figure 8. To obtain the spatial location information of fault development, digital extraction based on
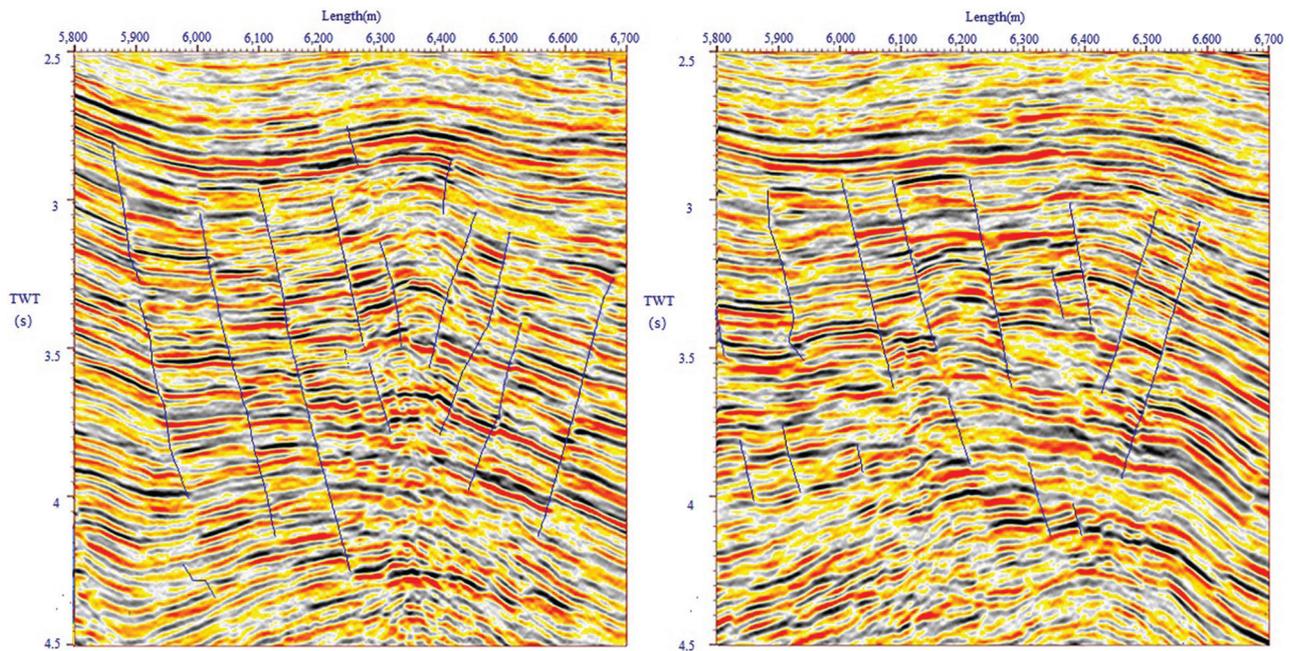
Figure 11. Imaging profile with manually picked fault curves
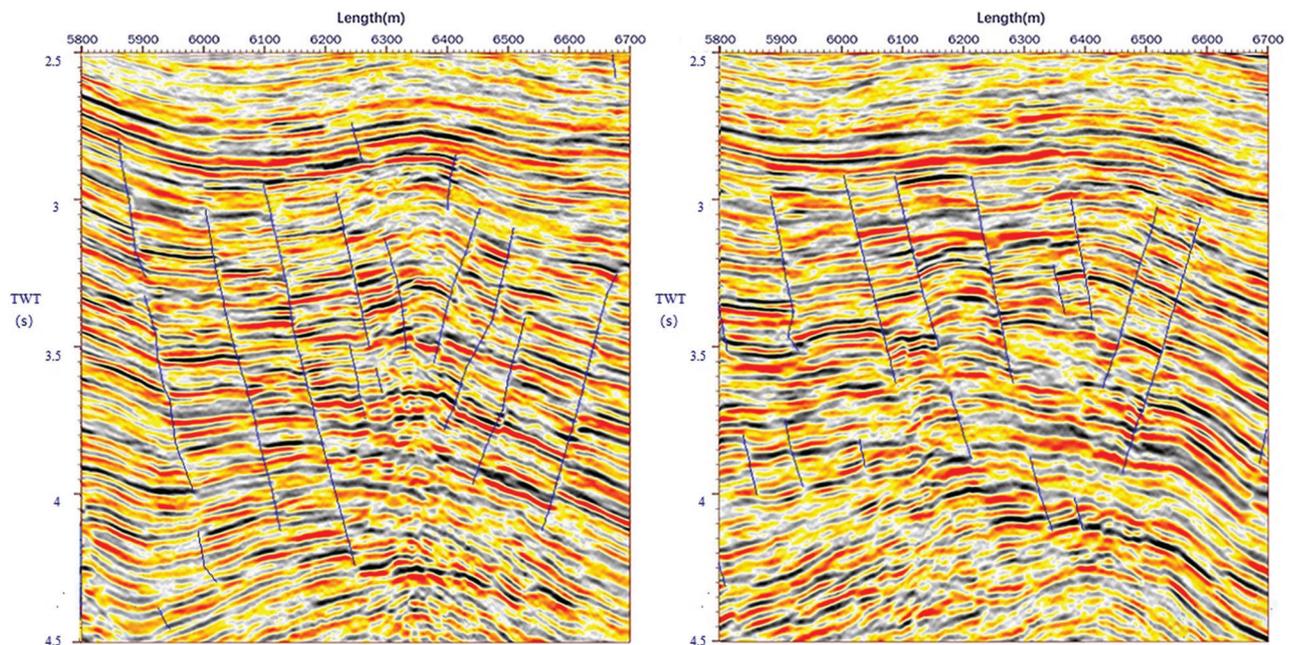Abbreviation: TWT: Two-way travel time.

Figure 12. Imaging profile with loaded fault curves
Abbreviation: TWT: Two-way travel time.

contour tracing technology was implemented, as illustrated by the colored curves on the profile shown in Figure 9.

For clarity, Figures 10-12 present the imaging profile, the manually picked fault curves, and the overlaid fault curves, respectively. A comparison shows that the main faults in the original profile have been effectively identified, and the fault curves picked by the proposed method are generally consistent with the manually picked ones in the vicinity of the fault structures, demonstrating the effectiveness
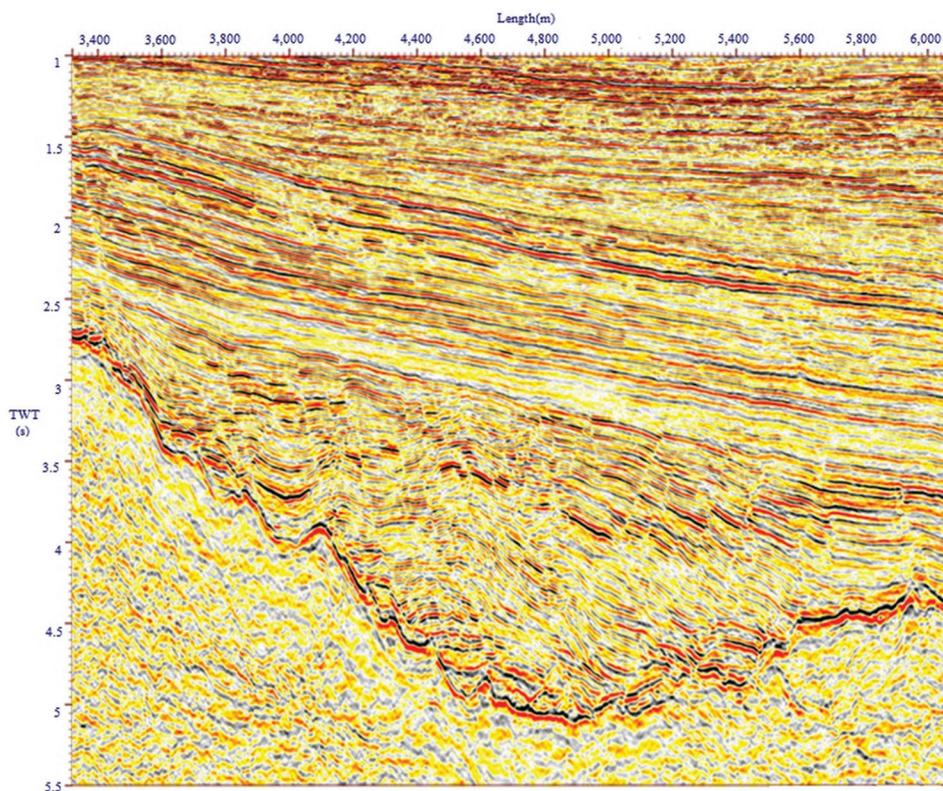
Figure 13. The original migrated section with unclear fault structures
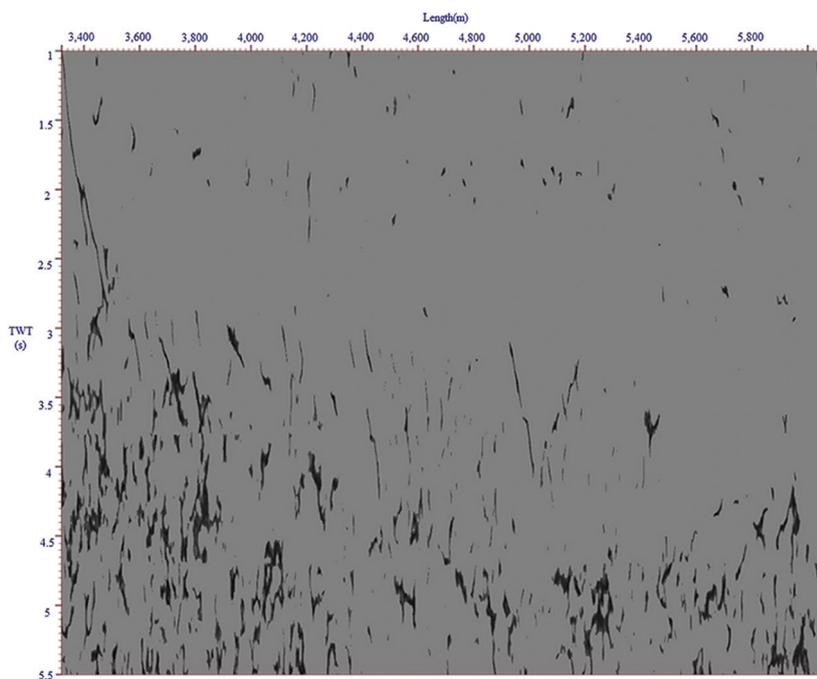Abbreviation: TWT: Two-way travel time.

Figure 14. Identified fault image
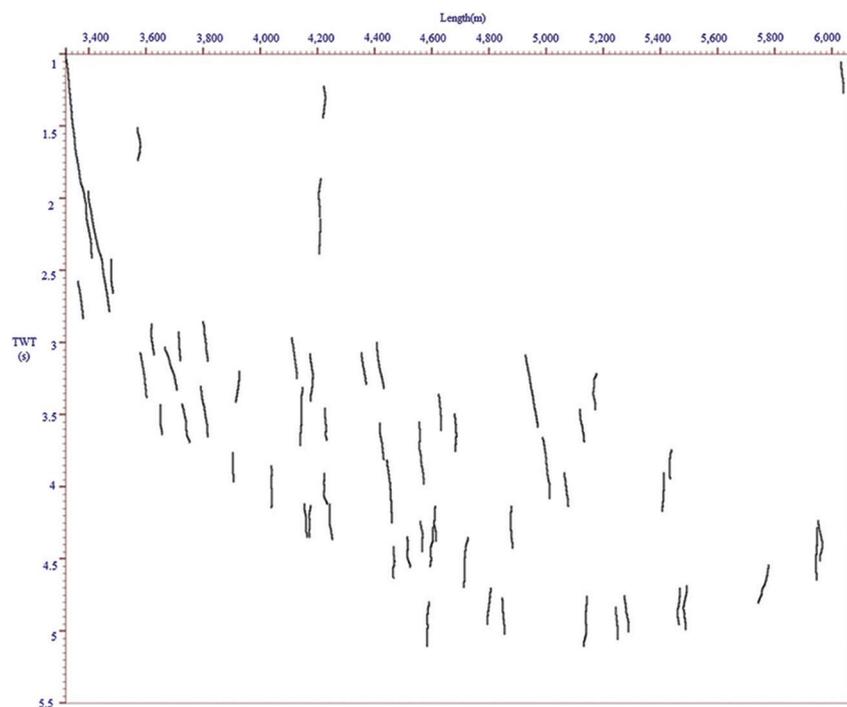Abbreviation: TWT: Two-way travel time.

Figure 15. Image of breakpoint list describing fault skeleton information
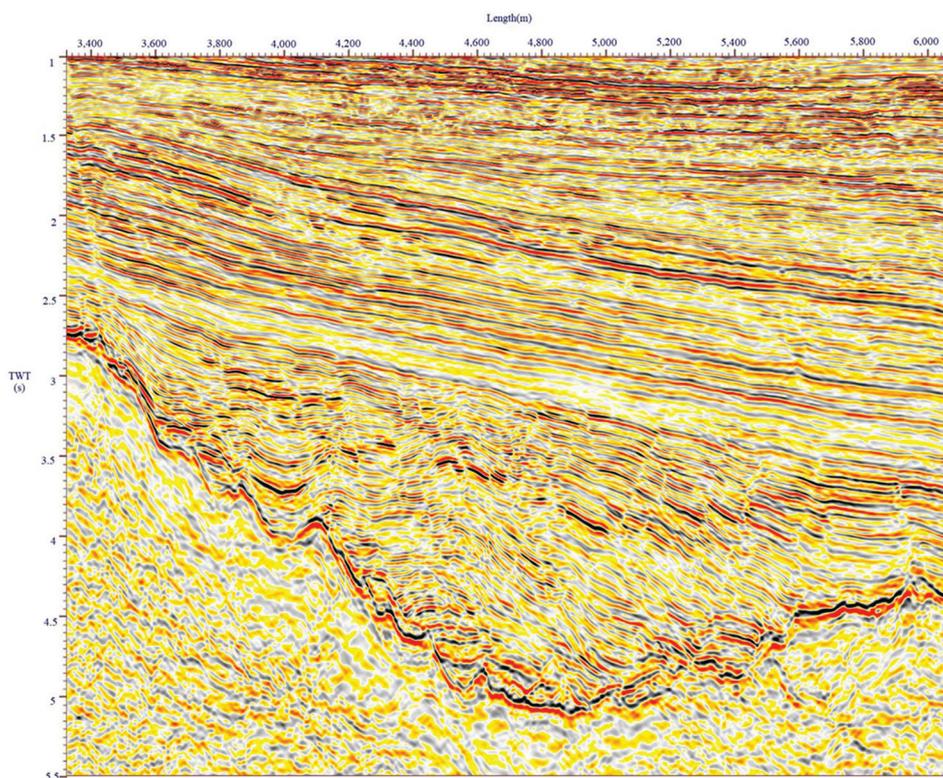Abbreviation: TWT: Two-way travel time.

Figure 16. Example of a denoised profile obtained using the curvelet transform
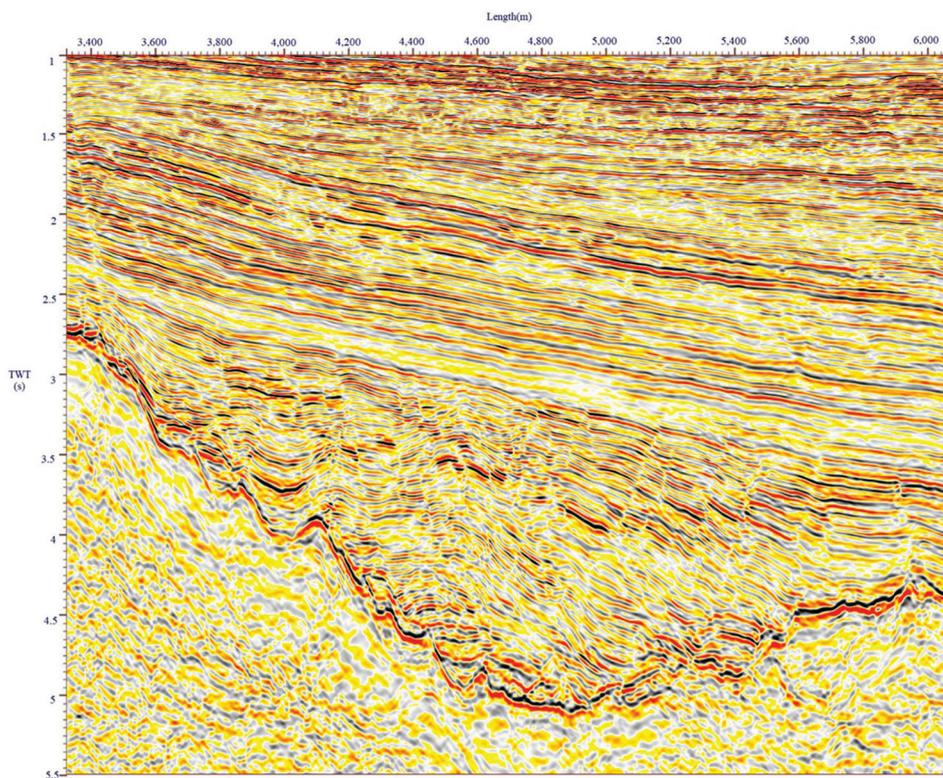Abbreviation: TWT: Two-way travel time.

Figure 17. Denoised profile with restored fault information
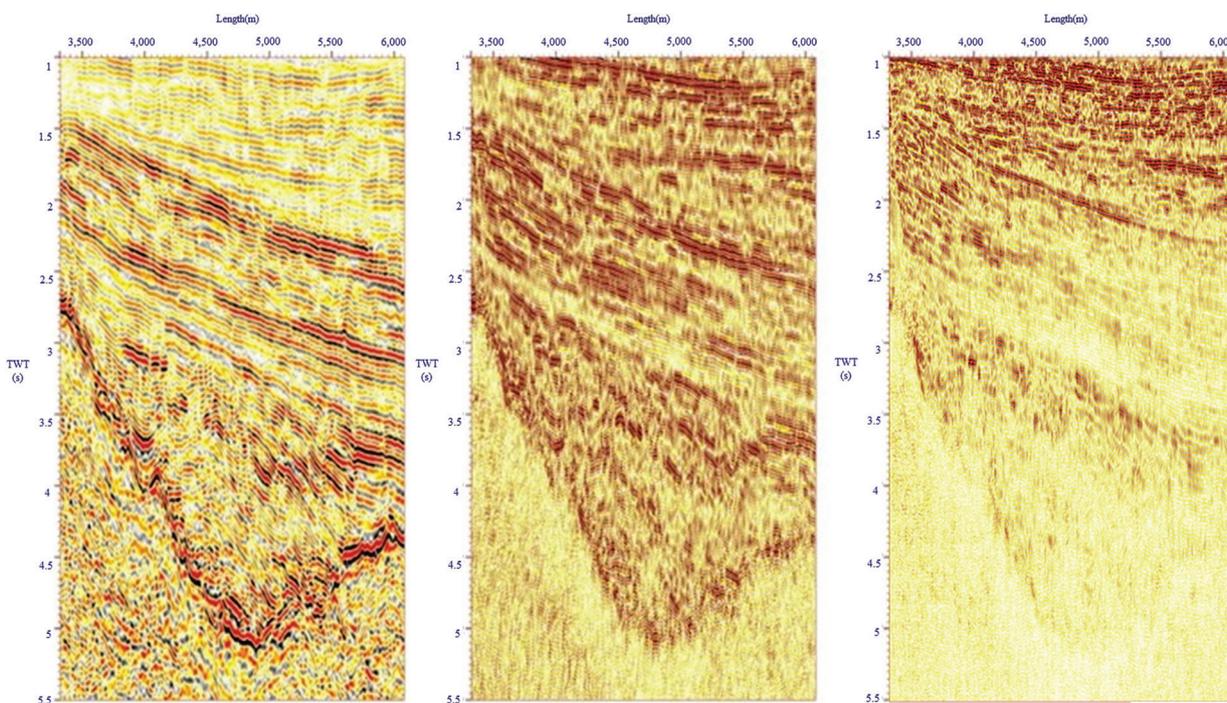Abbreviation: TWT: Two-way travel time.

Figure 18. Migrated the section of each scale component
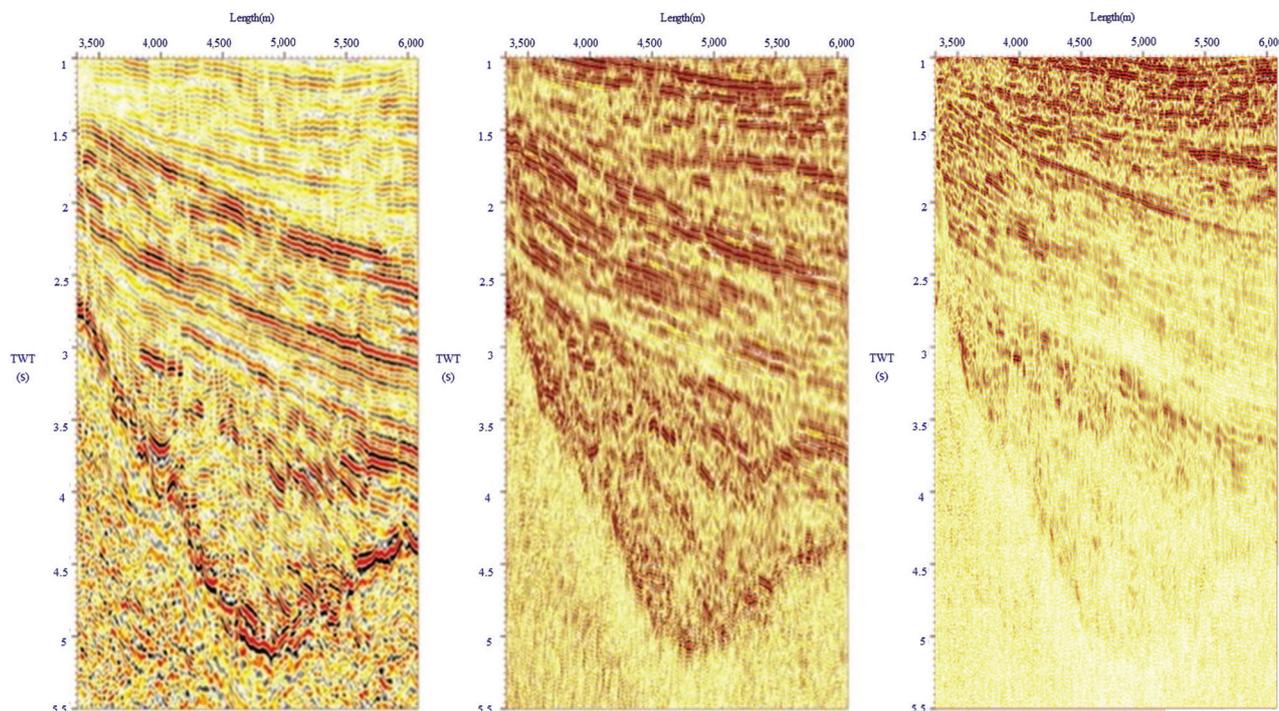Abbreviation: TWT: Two-way travel time.

Figure 19. Fault enhancement results for each scale component profile
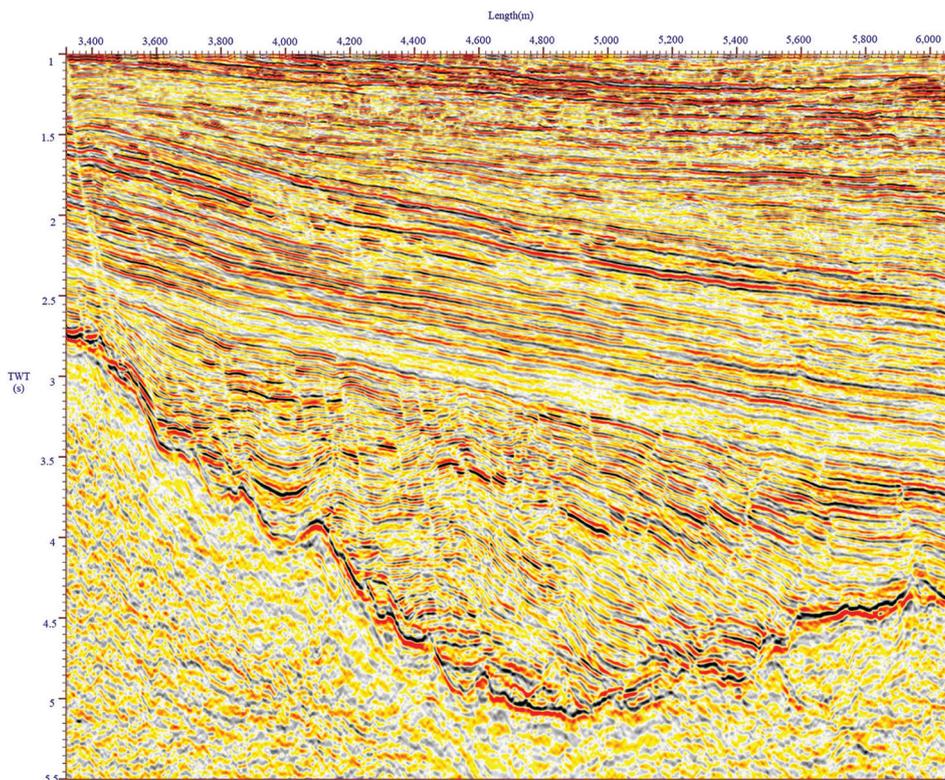Abbreviation: TWT: Two-way travel time.

Figure 20. Migrated section after fault enhancement
Abbreviation: TWT: Two-way travel time.

of the method. Our method achieved an accuracy of 97.63%, an F1 score of 93.24%, and an intersection over union of 80.64%. Overall, most metrics achieved the best performance among the compared methods, further demonstrating the reliability of the proposed approach.

To demonstrate the generalization performance of the trained neural network, we applied it to another work area for fault identification. The original migrated seismic section of the new work area, where the fault structures are not clearly visible, is shown in Figure 13. Using the trained neural network for identification, the resulting fault image is shown in Figure 14. Finally, the fault image was vectorized to obtain a profile describing the fault skeleton, as shown in Figure 15, for subsequent interpretation and analysis. The curves in the profile accurately indicate the spatial locations of fault development, demonstrating that our trained neural network has strong generalization capabilities.

4.2. Fault enhancement effect analysis of work area data

Based on **Equation 5**, the migrated section (Figure 13) was transformed into the curvelet domain. By setting the threshold parameter, the curvelet coefficients with values smaller than 0.1 were set to zero. Then, using **Equation 7**, the filtered result was transformed back to the time–space domain, resulting in the migrated section with attenuated random noise, as shown in Figure 16.

For the denoised migrated section shown in Figure 16, the fault information was restored based on the extracted breakpoint list (Figure 15) using **Equations 8** and **9**. The resulting profile is shown in Figure 17, where the discontinuities associated with the fault events are enhanced to a certain extent.

The denoised profile shown in Figure 17 was used, with the number of scales and directions for the curvelet transform set to 3 and 16, respectively. Using **Equation 11**, it was transformed into the curvelet domain. Subsequently, a single-scale component inverse transform was performed on the curvelet-domain records for scale indices $n = 1,2,$ or 3, resulting in the scale-component profiles shown in Figure 18. Through analysis, it can be observed that as the scale index n increases, the resolution of the component profiles improves, while the continuity of the faults gradually decreases.

For the migrated section of the three scale components shown in Figure 18, let g_1, g_2, and g_3 be 0, 0, and 0.5, respectively, and Δx_1, Δx_2, and Δx_3 be 225 m, 187.5 m, and 150 m, respectively. Based on **Equation 11**, the corresponding filtering factors were calculated. These factors were then used to perform fault-enhancement processing, and the resulting profiles are shown in

Figure 19. Overall, as the scale index n increases, the degree of fault filtering gradually decreases, achieving fault enhancement while preserving information.

The profile component data processed with differentiated parameters, as shown in Figure 19, were merged into a single migrated section. The resulting profile is shown in Figure 20. Compared to the original profile (Figure 13), the faults are significantly enhanced, providing a solid foundation for subsequent interpretation and analysis.

5. Conclusion

Our present focus is to demonstrate the feasibility and practical effectiveness of this U-Net–curvelet hybrid framework. The findings demonstrate that the hybrid framework effectively suppresses random noise and enhances the clarity of fault information, thereby further improving fault-identification accuracy. Applications to field data demonstrate that the method performs excellently under complex structural settings and low SNR conditions, enabling efficient and accurate fault identification, significantly improving fault imaging, and providing a reliable automated solution for seismic data interpretation.

However, direct quantitative comparisons with more complex architectures, such as U-Net–transformer models (e.g., MCA-SCUNet) were not conducted in this study. Nonetheless, we fully agree that further benchmarking with transformer-based models would provide valuable insight, and we consider this a key direction for future research. Future research should further optimize the network structure and explore more methods for integrating seismic attributes to address more complex geological conditions and exploration needs. Although the hybrid framework performs robustly on field data, challenges remain under very low SNR conditions: strong random/coherent noise tends to trigger false positives and obscure weak faults. Moreover, this method can be extended to the identification and enhancement of other geological features, further enhancing its applicability and practicality in geophysical exploration.

Conflict of interest

The authors declare no conflict of interest.

Author contributions

Conceptualization: All authors
Formal analysis: Jianhua Wang, Cong Niu, Yandong Wang, Yun Ling, Di Wang
Investigation: Jianhua Wang, Cong Niu, Yandong Wang, Yun Ling, Di Wang
Methodology: Jianhua Wang, Cong Niu, Yandong Wang, Yun Ling, Di Wang
Writing–original draft: Jianhua Wang, Cong Niu, Yandong Wang
Writing–review & editing: All authors

Availability of data

All data generated and analyzed during this study are included in this published article.

References

1. Marfurt KJ, Kirlin RL, Farmer SL, *et al*. 3-D seismic attributes using a semblance-based coherency algorithm. *Geophysics*. 1998;63(4):1150.

   doi: 10.1190/1.1444415

2. Gersztenkorn A, Marfurt KJ. Eigenstructure-based coherence computations as an aid to 3-D structural and stratigraphic mapping. *Geophysics*. 1999;64(5):1468-1479.

   doi: 10.1190/1.1444651

3. Li X, Yang P, Yan H, *et al*. Identification of minor fault and its applications on the development of offshore oil fields. *Comput Techn Geophys Geochem Explor*. 2014;36(2):222-227.

4. Roberts A. Curvature attributes and their application to 3D interpreted horizons. *First Break*. 2001;19(2):85-100.

   doi: 10.1046/j.0263-5046.2001.00142.x

5. Al-Dossary S, Marfurt KJ. 3D volumetric multispectral estimates of reflector curvature and rotation. *Geophysics*. 2006;71(5):P41-P51.

   doi: 10.1190/1.2242449

6. Hale D. Methods to compute fault images, extract fault surfaces, and estimate fault throws from 3D seismic images. *Geophysics*. 2013;78(2):O33-O43.

   doi: 10.1190/geo2012-0331.1

7. Wu X, Hale D. 3D seismic image processing for faults. *Geophysics*. 2016;81(2):IM1-IM11.

8. Pedersen SI, Randen, T, Sønneland L, *et al*. Automatic Fault Extraction using Artificial Ants. In: *SEG Technical Program Expanded Abstracts 2002, SEG-2002-0512*. Salt Lake City: SEG; 2002.

9. Lavialle O, Pop S, Germain C, *et al*. Seismic fault preserving diffusion. *J Appl Geophys*. 2007;61(2):132-141.

   doi: 10.1016/j.jappgeo.2006.06.002

10. Wu X, Fomel S. Automatic fault interpretation with optimal surface voting. *Geophysics*. 2018;83(5):O67-O82.

    doi: 10.1190/geo2018-0115.1

11. Chen G, Liu Y. Research progress of automatic fault recognition based on artificial intelligence. *Prog Geophys*. 2021;36(1):119-131.

12. He K, Zhang X, Ren S, Sun J. Deep Residual Learning for Image Recognition. In: *2016 IEEE Conference on Computer Vision and Pattern Recognition (CVPR)*; 2016. IEEE. p. 770-778.

    doi: 10.1109/CVPR.2016.90

13. Wu X, Shi Y, Fomel S, *et al*. Convolutional Neural Networks for Fault Interpretation in Seismic Images. In: *2018 SEG International Exposition and Annual Meeting*. Anaheim: SEG, 2018.

14. Long J, Shelhamer E, Darrell T. Fully convolutional networks for semantic segmentation. In: *2015 IEEE Conference on Computer Vision and Pattern Recognition (CVPR)*. IEEE; 2015. p. 3431-3440.

    doi: 10.1109/cvpr.2015.7298965

15. Ronneberger O, Fischer P, Brox T. *U-Net: Convolutional Networks for Biomedical image Segmentation[C]// Medical Image Computing and Computer-Assisted Intervention - MICCAI 2015*. Cham: Springer, 2015. p. 234-241.

    doi: 10.1007/978-3-319-24574-4_28.

16. Wu X, Liang L, Shi Y, *et al*. FaultSeg3D: Using synthetic data sets to train an end-to-end convolutional neural network for 3D seismic fault segmentation. *Geophysics*. 2019;84(3):IM35-IM45.

    doi: 10.1190/geo2018-0646.1

17. Zhao M, Zhao Y, Shen D, Wang J, Dai X. High-resolution processing of seismic data using adaptive attention mechanism U-net. *Oil Geophys Prospect*. 2024;59(4):675-683.

    doi: 10.13810/j.cnki.issn.1000-7210.2024.04.003

18. He T, Liu NH, Wu BY, *et al*. ResU-net based three-dimensional fault identification method and application. *Chin J Eng Math*. 2023;40(1):1-19.

    doi: 10.3969/j.issn.1005-3085.2023.01.001